nature geoscience

Article

https://doi.org/10.1038/s41561-023-01184-5

Recent state transition of the Arctic Ocean's Beaufort Gyre

Received: 19 June 2022

Accepted: 13 April 2023

Published online: 08 May 2023

Check for updates

Peigen Lin[1,2] ✉, Robert S. Pickart[2], Harry Heorton[3], Michel Tsamados[3], Motoyo Itoh[4] & Takashi Kikuchi[4]

The anti-cyclonic Beaufort Gyre is the dominant circulation of the Canada Basin and the largest freshwater reservoir in the Arctic Ocean. During the first part of the 2000s, the gyre intensified, expanded and accumulated freshwater. Using an extensive hydrographic dataset from 2003 to 2019, together with updated satellite dynamic ocean topography data, we find that over the past decade the Beaufort Gyre has transitioned to a quasi-stable state in which the increase in sea surface height of the gyre has slowed and the freshwater content has plateaued. In addition, the cold halocline layer, which isolates the warm/salty Atlantic water at depth, has thinned significantly due to less input of cold and salty water stemming from the Pacific Ocean and the Chukchi Sea shelf, together with greater entrainment of lighter water from the eastern Beaufort Sea. This recent transition of the Beaufort Gyre is associated with a southeastward shift in its location as a result of variation in the regional wind forcing. Our results imply that continued thinning of the cold halocline layer could modulate the present stable state, allowing for a freshwater release. This, in turn, could freshen the subpolar North Atlantic, impacting the Atlantic Meridional Overturning Circulation.

The Beaufort Gyre (BG) is the largest freshwater reservoir in the Arctic Ocean[1–3], driven by the anti-cyclonic winds in the Canada Basin[4]. Since 2000, the gyre has strengthened and its freshwater content (FWC) has increased by 40% relative to the 1970's climatology[5]. Associated with the accumulating freshwater, the gyre has expanded northwestward[6,7], and its layer of cold Pacific-origin water has widened laterally and thickened vertically[8]. There are many potential impacts of the changing BG on the hydrographic structure, physical processes and ecosystem of the Arctic, both local and remote. As such, it is of high interest to better understand the factors associated with such changes—including the underlying causes.

The gyre strength generally coincides with the intensity of the surface forcing[3,9], which is a combination of the wind–ocean stress (or simply wind stress) and the ice–ocean stress[10,11]. As the gyre spins up, the acceleration of the geostrophic circulation reduces the ice–ocean stress, which in turn weakens the forcing and acts to stabilize the gyre[12]. Another negative feedback with respect to forcing is that the growing FWC and enhanced halocline tilting generate more eddies via baroclinic instability, which in turn dampen the gyre and flatten the halocline[13]. Both modelling and satellite sea surface height measurements have suggested that the BG stabilized from 2008 to 2014[9,14]. However, it is unknown if this represented an overall change in the state of the gyre. Furthermore, the underlying reasons for any such change have not been addressed observationally.

A major source of the interannual variation in FWC of the BG is the Pacific-origin water entering through the Bering Strait[5]. A substantial portion of this water is subsequently fluxed off the Chukchi shelf through Barrow Canyon[15], and ultimately enters the gyre[16–18]. River runoff, particularly from the Mackenzie River, is believed to contribute nearly equally to the interannual variation[5,19]. Our study investigates the long-term

[1]School of Oceanography, Shanghai Jiao Tong University, Shanghai, China. [2]Woods Hole Oceanographic Institution, Woods Hole, MA, USA. [3]Department of Earth Sciences, Centre for Polar Observation and Modelling, University College London, London, UK. [4]Institute of Arctic Climate and Environment Research, Japan Agency for Marine-Earth Science and Technology, Yokosuka, Japan. ✉e-mail: plinwhoi@gmail.com

trends of the BG and reveals that it has transitioned to a quasi-stable state over the past decade. We use an extensive updated collection of historical hydrographic data and satellite dynamic ocean topography (DOT) data to characterize this state and provide insights into the reasons for the change. We quantify the evolution of the gyre in terms of its sea surface height and FWC, and explore the connection to the cold halocline layer (CHL). As the gyre has evolved to its recent state, the halocline has thinned considerably, the causes of which are addressed.

Long-term trend of the BG

The state of BG is reflected by the DOT averaged over the BG region (Fig. 1a; see Extended Data Fig. 1 for the DOT climatology). The newly updated DOT data presented here extend the time series to 2019. The spatially averaged DOT of the BG generally increased from 2003 to 2019 (Fig. 1b), but there are notable variations around this trend. We divide the record into two time periods: 2003–2011 and 2012–2019. The break point was objectively chosen by computing the trends corresponding to a four-year running window over the DOT time series. It revealed that the trend reaches a minimum (close to zero) in the period 2010–2013 (the results are not sensitive to a one-year shift in the break point). In the first period, there was a strong increase in the average DOT throughout the BG region, with a maximum trend in the northwest Canada Basin where the gyre expanded to (Fig. 2a; consistent with a previous result[7]). Since that time, the BG has continued to strengthen, but at a considerably slower rate (with a short weakening from 2011 to 2013; Fig. 1b). Unlike the earlier period, the increase in DOT occurred predominantly in the southeast part of the Canada Basin (Fig. 2c). Meanwhile, a decreasing trend is found west of the Chukchi Plateau. These changes indicate that, over the past decade, the BG has contracted and shifted to the southeast part of the basin (see also Extended Data Fig. 2). We note that, while a large part of this shift occurred in 2019, the trend is still significant when excluding that year.

To illustrate how the FWC has varied in relation to the changes in the strength of the BG, we calculated the annual mean FWC using the historical hydrographic data (FWC_1 in the Methods; Fig. 1c). To compare with previous studies, we also computed the freshwater volume as the FWC multiplied by the area of the BG region. The FWC was approximately 14.6 m in 2003 and increased to more than 20 m in 2011, equivalent to an increase in freshwater volume from 16,000 km^3 to more than 22,000 km^3 (consistent with previous observational estimates[1]). This corresponds to a trend of 940 $km^3\ yr^{-1}$. However, the situation changed dramatically in the second period when the freshwater volume underwent fluctuations between 22,000 km^3 and 24,000 km^3. During this time there was no statistically significant trend. We also constructed a time series of FWC using the DOT data together with estimates of the ocean mass (FWC_2 in the Methods), as well as the associated freshwater volume. These two FWC estimates are in phase with each other ($r = 0.92$, $P < 0.01$) and have comparable trends, indicating that the BG has entered a quasi-stable regime whereby the increase of the DOT has slowed and the FWC has plateaued.

Thinning of the CHL

We now investigate the response of the water column in the BG region during the second period. Beneath the surface layer, the halocline acts to inhibit upward mixing of the warm deep Atlantic water that otherwise could result in substantial ice melt[1]. In the western Arctic, the warm halocline, which originates from the Pacific summer water[4,18], sits atop the cold halocline, which is ventilated by cold and salty winter water formed/modified locally on the shelves of the Chukchi and Beaufort seas via brine rejection[20,21]. The warm halocline layer corresponds to a practical salinity (S) range of 28–32.6, while the CHL spans the range 32.6–33.9. These ranges were identified using mean vertical profiles within the BG (see Methods).

We computed trends in the volume of water within salinity classes spanning the warm and cold haloclines in the BG region for the two periods considered above (Fig. 3). In the first period, the trends are positive for $S > 30$, particularly in the CHL. The thickening halocline coincides with the increasing DOT in the early period (Fig. 1b). By contrast, the trends are significantly negative in the CHL in the later period, peaking at $-600\ km^3\ yr^{-1}$ for waters with $S \approx 33$, while the trends remain relatively close to zero at shallower depths. This suggests that the thinning of the CHL results in the thinning of the entire halocline. One might then ask, what is the impact of changes in the thickness of the CHL on the layer thickness of the entire freshwater reservoir lying above the Atlantic water?

To address this, we constructed thickness anomaly time series, relative to the value in 2003, for the following: (1) the CHL layer; (2) the layer from the surface to the top of the CHL (comprising the warm halocline and the surface layer); and (3) the sum of these two; that is, the full layer above the underlying Atlantic water (Fig. 1d). Associated with the changes of DOT and FWC, the full layer thickened markedly by $5.8\ m\ yr^{-1}$ in the early period, due mostly to thickening of the layer above the CHL, although the CHL did undergo a net expansion during this period. By contrast, since 2012 the CHL has been thinning at a rate of $-1.5\ m\ yr^{-1}$, offsetting the expansion of the upper layer and causing a plateau in total thickness. The steric effect of the plateaued layer plays a role in the slower increase in DOT[22]. This trend in the thickness of the CHL has not been spatially uniform, however (Fig. 2e): while thinning has occurred over a large portion of the BG region, particularly west of the Chukchi Plateau, the layer has thickened in the southeast portion of the Canada Basin. This agrees well with the spatial trends of DOT and FWC during the second period (Fig. 2c,d).

It has been argued that the relocation and expansion of the BG during the early period was caused primarily by the strengthening atmospheric Beaufort High and its enhanced negative wind stress curl[7,9]. To further investigate the role of atmospheric forcing during the second period, we constructed a map of the trend of wind stress curl from 2012 to 2019 (Fig. 2f). A negative trend of wind stress curl is evident in the southeast part of the Canada Basin where the DOT, FWC and CHL thickness have increased. This makes sense dynamically in that enhanced negative wind stress curl leads to stronger Ekman pumping, which in turn causes these changes. At the same time, the negative trends of DOT, FWC and CHL thickness to the west of the Chukchi Plateau are likely associated with the positive trend of wind stress curl in this region. This highlights the interconnectedness of the different attributes of the BG and their relationship to the atmospheric Beaufort High.

Fig. 1 | Long-term trends of the BG: 2003–2011 versus 2012–2019. **a**, Geographic map of the Arctic Ocean with an enlarged view of the study region (black box). The schematic BG is marked by the yellow circle. The BG region is delimited by 130–180° W, 81° N and 300 m isobath (thick purple line), over which area averages (± standard errors) are computed, shown in **b**–**d**. The bathymetry from the International Bathymetric Chart of the Arctic Ocean v3 is coloured, with the isobaths of 40, 70, 150, 250, 500 m in grey, and 100 and 300 m highlighted in black. **b**, The annual mean BG DOT (m). **c**, The annual mean BG FWC (m) and volume ($\times 10^4\ km^3$) estimated using the historical hydrographic data (FWC_1, magenta) and using the DOT + GRACE data (FWC_2, green). **d**, The annual mean BG thickness anomalies (m) relative to 2003 of the layer from the surface to the top of the cold halocline (yellow), the CHL beneath this (purple) and the sum of the two layers (orange). The standard error, shown by the bars, is the standard deviation divided by square root of the degrees of freedom, where the degrees of freedom for each year (ranging from 12 to 71) are computed using an integral timescale of three days for the hydrographic data and one month for the monthly satellite data. The dashed lines are the linear trends in the early and late periods, and the black lines in **b** and **c** denote the linear trends of DOT and FWC_1 over the full study period, respectively. The trends were computed using the time series of annual mean variables.

https://doi.org/10.1038/s41561-023-01184-5

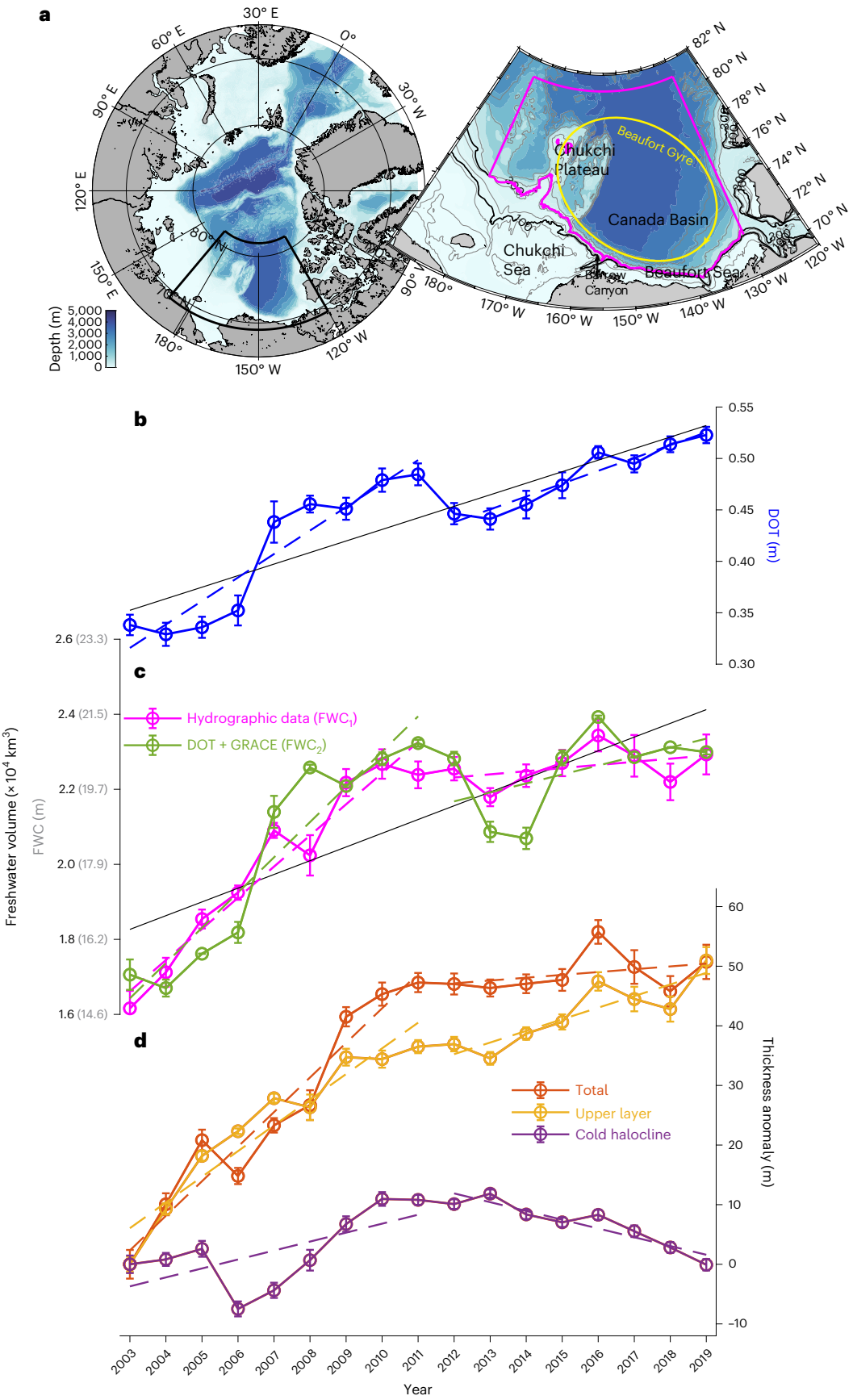

https://doi.org/10.1038/s41561-023-01184-5

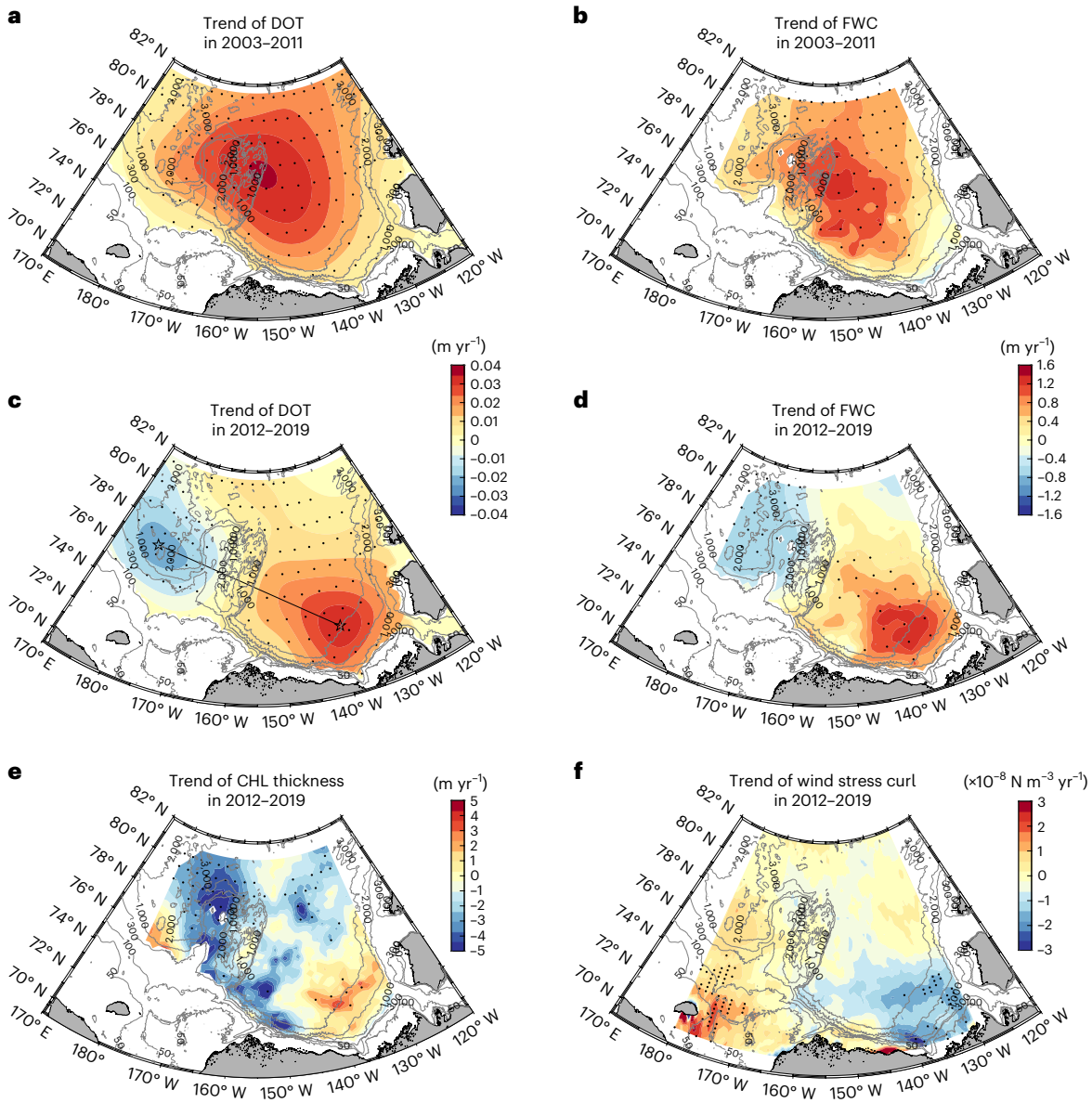

Fig. 2 | Spatial distribution of the trends in the BG region. a–**f**, Trends of DOT in the early period (2003–2011; **a**) and in the late period (2012–2019; **c**); trends of the FWC in the early period (**b**) and in the late period (**d**); and trends of the thickness of the CHL (**e**) and the wind stress curl (**f**) in the late period. The dots represent the areas with statistically significant trends (subsampled every five points for the DOT data, every four points for the FWC and CHL thickness, and every five points in longitude for the wind stress curl). The line connecting the two centres of the trends (76.78° N, 179.6° W and 72.87° N, 139.37° W) in **c** is used to construct the Hovmöller plot in Fig. 4a.

Causes of the thinning CHL

Pacific-origin winter water is the main source water that ventilates the CHL in the western Arctic Ocean[8,18]. Concomitant with the increased Bering Strait inflow, the Pacific water has become markedly warmer and fresher. These changes suggest that the Pacific winter water, which previously ventilated the CHL in the 1990s, probably now more readily affects the shallower layer in the basin[23]. This is in line with our results showing the recent thinning of the CHL and the thickening of the layer immediately above (Fig. 3). However, as the Pacific winter water transits across the Chukchi shelf, its salinity can be increased via brine rejection during ice formation in polynyas and leads[20,24,25]. Hence, it is unclear how these offsetting effects have been playing out. As a substantial portion of Pacific-origin water flows into the basin through Barrow Canyon, we now use mooring data at the canyon mouth to further elucidate the source water that eventually impacts the CHL in the BG region.

Figure 3 shows the trends of the volume of water fluxed off the shelf through Barrow Canyon in each salinity class through the water column. One sees that in both periods the trends of the Barrow Canyon outflow are in line with the volume trends in the basin computed above; in particular, positive trends in the CHL from 2003 to 2011, peaking above the CHL layer, and negative trends from 2012 to 2019, with the maximum near a salinity of 33 within the CHL. Note, however, that the trends of the Barrow Canyon outflow water that supplies the CHL are smaller than the ones in the basin (although they are not significantly different), and the discrepancy is greater in the later years. These results thus indicate two important aspects regarding ventilation in the basin: the Barrow Canyon outflow water cannot solely explain the total trend of the CHL in the BG, and the contribution from the canyon is reduced in the later years.

Cold and salty winter water is also regularly formed along the eastern Beaufort Sea (EBS) shelf and fluxed offshore by downwelling[21]. It has been previously emphasized that the contribution of freshwater from

https://doi.org/10.1038/s41561-023-01184-5

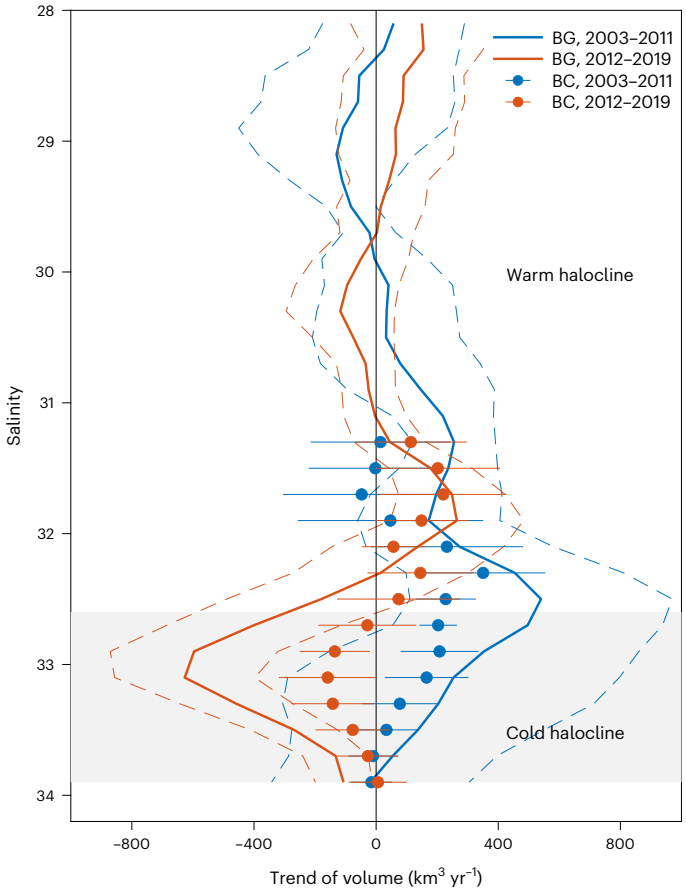

Fig. 3 | Linear trends of volume within salinity classes in relation to the source water. Trends of volume in the BG region (curves) and in the main source water at the mouth of Barrow Canyon (BC, filled circles), in the early period (2003–2011, blue) and the late period (2012–2019, orange). The 95% confidence intervals of the trends are denoted by the dashed lines and horizontal bars. The shaded region is the CHL.

the EBS is comparable to the Pacific-origin water[5]. It is thus reasonable to consider the winter water formed in the EBS as the other important source water of the CHL in the BG, and how this source water might respond to the spatial change of the BG. It is worth noting that the Barrow Canyon outflow can feed the EBS via the eastward-flowing Beaufort shelfbreak jet[26]. However, the jet is centred near the 150 m isobath and is bottom-intensified in the mean, particularly in the cold months[27], and thus it has a minor impact on the winter water on the shelf.

To investigate the impact of the eastern source of winter water in the different BG regimes, we conducted Lagrangian particle experiments based on the annual mean velocity field averaged over the CHL from the global eddy-resolving physical ocean and sea ice reanalysis (GLORYS12) product (the GLORYS12 velocities show good agreement with mooring data in the western Arctic; Extended Data Fig. 3). The first experiment was done for the extreme year of 2011, at the end of the early period when the DOT core of the BG was located at its northwestern-most location during this period (Fig. 4a; note that the BG reached the extreme northwestern position in 2013). Particles denoted by blue and red colours were released along the 100 m isobath in the Chukchi Sea/western Beaufort Sea (CS/WBS) and EBS, respectively (Fig. 4b). After one year, most of the CS/WBS particles progressed into the BG region near the Chukchi Plateau. The majority of these parcels emanated from the eastern side of Barrow Canyon and subsequently turned to the west, consistent with previous observational and modelling studies[28,29]. By contrast, most of the EBS particles stayed very close to the location where they were released. To quantify this, we computed the percentage of the CS/WBS and EBS particles that resided for more than half the year in the BG region (within the purple polygon in Fig. 1a). This revealed that 90% of the CS/WBS particles did so, compared with only 15% of the EBS particles.

A second experiment was then conducted for the extreme year of 2019, at the end of the later period when the DOT core of the BG had shifted to the southeastern-most location during this period (Fig. 4a). In this case, 84% of the CS/WBS particles progressed into the BG region near the Chukchi Plateau, slightly less than the first experiment. However, the percentage of EBS particles reaching this region increased dramatically to 73%. This suggests that the contribution of the EBS water to the CHL is dynamically linked to the BG state: when the gyre shifts to the southeast, the CHL is more likely to be readily ventilated by winter water emanating from the EBS shelf.

The question remains as to the role of the EBS water in the thinning of the CHL. To address this, we used the historical hydrographic data and computed the fractional occurrence of the water in each of the salinity classes of Fig. 3 on the EBS shelf (128–147° W and shoreward of 100 m isobath) and on the CS/WBS shelf (147–165° W, shoreward of 100 m isobath and extending southward to 70.5° N or to the coast). This revealed that, for the warm halocline layer, the fractional occurrence was similar for the two regions, while for the CHL the fractional occurrence was larger on the CS/WBS shelf. This, together with the fact that the area of the CS/WBS shelf is greater than that of the EBS, implies that the potential source volume of water that can ventilate the CHL is larger on the CS/WBS shelf. Assuming that the CHL source water in the EBS originates from the inner shelf[21], it gives a volume supply of ~400 km^3, substantially less than the annual mean volume of the water fluxed via Barrow Canyon, ~2,400 km^3, estimated from the moorings. Hence, during the second period when there is enhanced influence from the EBS (Fig. 4c), the amount of available shelf water in the salinity class of the CHL is less, implying that the CHL would thin. We conclude then that both the reduced Barrow Canyon outflow and the southeast shift in the BG location led to the reverse in trend of the CHL thickness from the early to the late period.

Implications of the recent BG state

Our results have demonstrated that, during the past decade, the BG has transitioned to a quasi-stable state, shifting towards the southeast Canada Basin where the negative wind stress curl has intensified, together with a dampened rate of increase of sea surface height, stabilization of FWC and thinning of the CHL. The recent decrease in the amount of Pacific-origin winter water exiting Barrow Canyon explains some of the CHL thinning, while the enhanced influence from the EBS—due to the southeastward shift of the BG—likely contributes as well.

Previous work has demonstrated that the local wind patterns modulating the BG are related to the large-scale Arctic Oscillation[4]. On interannual timescales, positive Arctic Oscillation states are associated with a contracted BG situated in the southeast Canada Basin, while negative Arctic Oscillation states correspond to an expanded BG. A similar relationship holds on decadal timescales, with a northwestward expansion and movement during 2003–2011 when the Arctic Oscillation index was mostly negative, and southeastward shift during 2012–2019 when the Arctic Oscillation was mainly in the positive state (Extended Data Fig. 4). We emphasize, however, that the recent state of the BG documented here does not represent a return to the initial condition of 2003 when the gyre was weak and located partially in the southeastern basin. Instead, under the strengthened wind stress curl, the gyre has continuously intensified even though it has contracted (Fig. 4a), and it has maintained its excess freshwater storage. That said, with a steric effect of the continued thinning of the CHL due to a decrease in the source winter water, the DOT of the gyre may be further stabilized or perhaps begin to drop, disrupting the freshwater accumulation in the gyre. A recent study has shown

https://doi.org/10.1038/s41561-023-01184-5

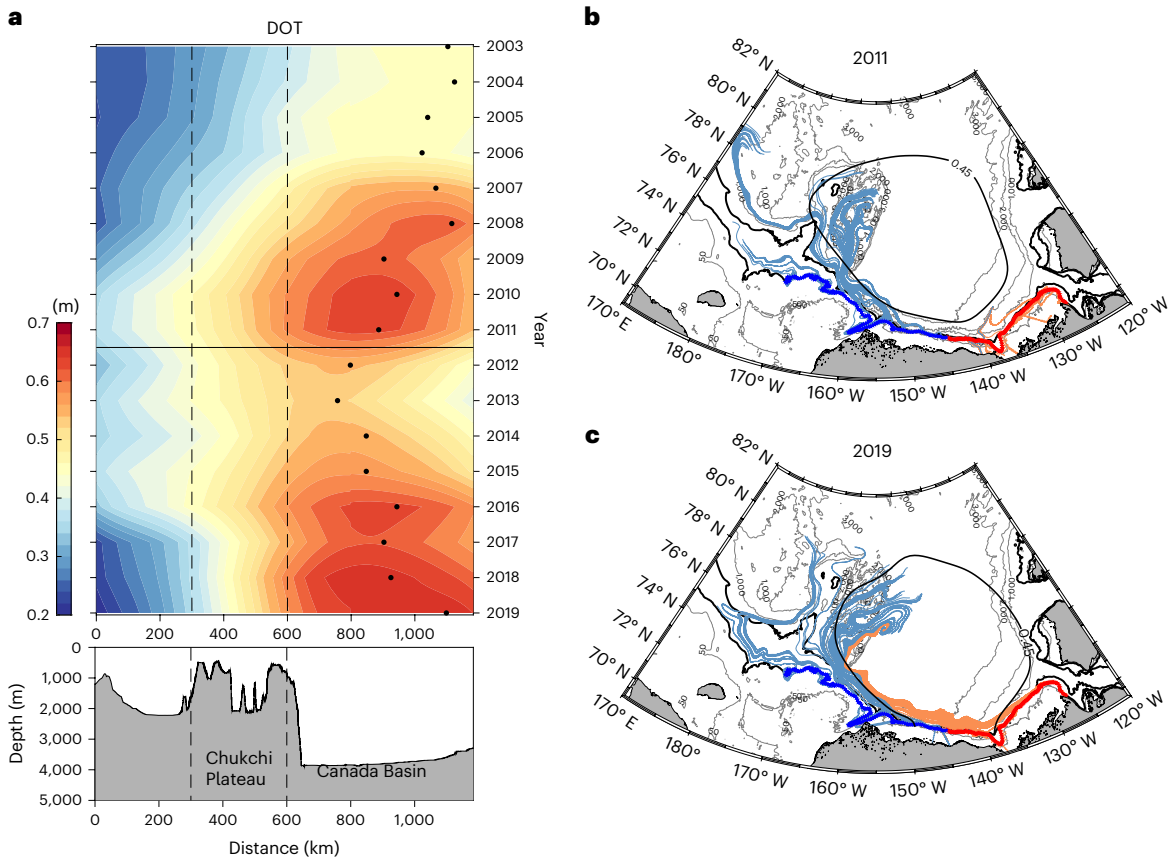

Fig. 4 | Inferred contributions to the CHL in the BG region. a, Hovmöller diagram of DOT (m) along the line in Fig. 2c from 2003 to 2019 (upper panel), with the dots denoting the maximum DOT projected onto the line in each year, and the horizontal solid line separating the two time periods. The associated bathymetry is shown (bottom panel), where the east and west edges of the Chukchi Plateau are denoted by the vertical dashed lines. **b**, The Lagrangian particle experiment in 2011. The 0.45 m DOT contour representing the location of the BG is shown (black curve). The particles are released along the 100 m isobath in the CS/WBS (blue stars) and in the EBS (red stars). The trajectories of the particles after one year are coloured light blue for the CS/WBS and light red for the EBS. **c**, Same as **b**, but for the experiment in 2019.

that the FWC in the gyre slightly dropped in 2020–2021[30]. If these conditions continue going forward, it could cause a pronounced salinity anomaly to progress through the Canadian Arctic Archipelago into the Labrador Sea and/or through the Fram Strait into the Nordic seas[31–33]. It is argued that half of the freshwater from the Arctic is diverted into the north Atlantic interior, providing the major source of freshening in the Atlantic Meridional Overturning Circulation, while the other half joins the estuarine circulation along the boundary[34]. As was the case with the Great Salinity Anomaly[35], as well as with the recent major freshening event from 2012 to 2016[36], this will probably impede wintertime convection, which could impact the Atlantic Meridional Overturning Circulation[37], a key component of global climate[38].

Online content

Any methods, additional references, Nature Portfolio reporting summaries, source data, extended data, supplementary information, acknowledgements, peer review information; details of author contributions and competing interests; and statements of data and code availability are available at https://doi.org/10.1038/s41561-023-01184-5.

References

1. Proshutinsky, A., Krishfield, R. & Timmermans, M. L. Introduction to special collection on Arctic Ocean modeling and observational synthesis (FAMOS) 2: Beaufort Gyre phenomenon. *J. Geophys. Res. Oceans* **125**, e2019JC015400 (2020).
2. Proshutinsky, A. et al. Beaufort Gyre freshwater reservoir: state and variability from observations. *J. Geophys. Res. Oceans* **114**, C00A10 (2009).
3. Timmermans, M. L. & Marshall, J. Understanding Arctic Ocean circulation: a review of ocean dynamics in a changing climate. *J. Geophys. Res. Oceans* **125**, e2018JC014378 (2020).
4. Steele, M. et al. Circulation of summer Pacific halocline water in the Arctic Ocean. *J. Geophys. Res. Oceans* **109**, C02027 (2004).
5. Proshutinsky, A. et al. Analysis of the Beaufort Gyre freshwater content in 2003–2018. *J. Geophys. Res. Oceans* **124**, 9658–9689 (2019).
6. Armitage, T. W. et al. Arctic Ocean surface geostrophic circulation 2003–2014. *Cryosphere* **11**, 1767–1780 (2017).
7. Giles, K. A., Laxon, S. W., Ridout, A. L., Wingham, D. J. & Bacon, S. Western Arctic Ocean freshwater storage increased by wind-driven spin-up of the Beaufort Gyre. *Nat. Geosci.* **5**, 194–197 (2012).
8. Zhong, W., Steele, M., Zhang, J. & Cole, S. T. Circulation of Pacific winter water in the western Arctic Ocean. *J. Geophys. Res. Oceans* **124**, 863–881 (2019).
9. Regan, H. C., Lique, C. & Armitage, T. W. The Beaufort Gyre extent, shape, and location between 2003 and 2014 from satellite observations. *J. Geophys. Res. Oceans* **124**, 844–862 (2019).
10. Tsamados, M. et al. Impact of variable atmospheric and oceanic form drag on simulations of Arctic sea ice. *J. Phys. Oceanogr.* **44**, 1329–1353 (2014).

11. Yang, J. The seasonal variability of the Arctic Ocean Ekman transport and its role in the mixed layer heat and salt fluxes. *J. Clim.* **19**, 5366–5387 (2006).
12. Meneghello, G., Marshall, J., Timmermans, M.-L. & Scott, J. Observations of seasonal upwelling and downwelling in the Beaufort Sea mediated by sea ice. *J. Phys. Oceanogr.* **48**, 795–805 (2018).
13. Manucharyan, G. E. & Spall, M. A. Wind-driven freshwater buildup and release in the Beaufort Gyre constrained by mesoscale eddies. *Geophys. Res. Lett.* **43**, 273–282 (2016).
14. Zhang, J. et al. The Beaufort Gyre intensification and stabilization: a model-observation synthesis. *J. Geophys. Res. Oceans* **121**, 7933–7952 (2016).
15. Itoh, M., Nishino, S., Kawaguchi, Y. & Kikuchi, T. Barrow Canyon volume, heat, and freshwater fluxes revealed by long-term mooring observations between 2000 and 2008. *J. Geophys. Res. Oceans* **118**, 4363–4379 (2013).
16. Lin, P., Pickart, R. S., Moore, G., Spall, M. A. & Hu, J. Characteristics and dynamics of wind-driven upwelling in the Alaskan Beaufort Sea based on six years of mooring data. *Deep Sea Res. II* **162**, 79–92 (2019).
17. Lin, P., Pickart, R. S., Våge, K. & Li, J. Fate of warm Pacific water in the Arctic Basin. *Geophys. Res. Lett.* **48**, e2021GL094693 (2021).
18. Timmermans, M. L., Marshall, J., Proshutinsky, A. & Scott, J. Seasonally derived components of the Canada Basin halocline. *Geophys. Res. Lett.* **44**, 5008–5015 (2017).
19. Krishfield, R. A. et al. Deterioration of perennial sea ice in the Beaufort Gyre from 2003 to 2012 and its impact on the oceanic freshwater cycle. *J. Geophys. Res. Oceans* **119**, 1271–1305 (2014).
20. Itoh, M. et al. Interannual variability of Pacific winter water inflow through Barrow Canyon from 2000 to 2006. *J. Oceanogr.* **68**, 575–592 (2012).
21. Lin, P. et al. On the nature of wind-forced upwelling and downwelling in Mackenzie Canyon, Beaufort Sea. *Prog. Oceanogr.* **198**, 102674 (2021).
22. Stammer, D. Steric and wind-induced changes in TOPEX/Poseidon large-scale sea surface topography observations. *J. Geophys. Res. Oceans* **102**, 20987–21009 (1997).
23. Woodgate, R. A. & Peralta-Ferriz, C. Warming and freshening of the Pacific inflow to the Arctic from 1990–2019 implying dramatic shoaling in Pacific winter water ventilation of the Arctic water column. *Geophys. Res. Lett.* **48**, e2021GL092528 (2021).
24. Pacini, A. et al. Characteristics and transformation of Pacific winter water on the Chukchi Sea shelf in late spring. *J. Geophys. Res. Oceans* **124**, 7153–7177 (2019).
25. Pickart, R. S. et al. Circulation of winter water on the Chukchi shelf in early summer. *Deep Sea Res. II* **130**, 56–75 (2016).
26. Lin, P. et al. Circulation in the vicinity of Mackenzie Canyon from a year-long mooring array. *Prog. Oceanogr.* **187**, 102396 (2020).
27. Nikolopoulos, A. et al. The western Arctic boundary current at 152° W: structure, variability, and transport. *Deep Sea Res. II* **56**, 1164–1181 (2009).
28. Leng, H., Spall, M. A., Pickart, R. S., Lin, P. & Bai, X. Origin and fate of the Chukchi slope current using a numerical model and in-situ data. *J. Geophys. Res. Oceans* **126**, 2021JC017291 (2021).
29. Li, M. et al. Circulation of the Chukchi Sea shelfbreak and slope from moored timeseries. *Prog. Oceanogr.* **172**, 14–33 (2019).
30. Timmermans, M.-L. & Toole, J. M. The Arctic Ocean's Beaufort Gyre. *Annu. Rev. Mar. Sci.* **15**, 223–248 (2023).
31. Karpouzoglou, T., de Steur, L., Smedsrud, L. H. & Sumata, H. Observed changes in the Arctic freshwater outflow in Fram Strait. *J. Geophys. Res. Oceans* **127**, e2021JC018122 (2022).
32. Rudels, B. Volume and freshwater transports through the Canadian Arctic Archipelago-Baffin Bay system. *J. Geophys. Res. Oceans* **116**, C00D10 (2011).
33. Zhang, J. et al. Labrador Sea freshening linked to Beaufort Gyre freshwater release. *Nat. Commun.* **12**, 1229 (2021).
34. Le Bras, I. et al. How much Arctic fresh water participates in the subpolar overturning circulation? *J. Phys. Oceanogr.* **51**, 955–973 (2021).
35. Gelderloos, R., Straneo, F. & Katsman, C. A. Mechanisms behind the temporary shutdown of deep convection in the Labrador Sea: lessons from the Great Salinity Anomaly years 1968–71. *J. Clim.* **25**, 6743–6755 (2012).
36. Holliday, N. P. et al. Ocean circulation causes the largest freshening event for 120 years in eastern subpolar North Atlantic. *Nat. Commun.* **11**, 585 (2020).
37. Lazier, J. R. Oceanographic conditions at ocean weather ship *Bravo*, 1964–1974. *Atmos. Ocean* **18**, 227–238 (1980).
38. Haine, T. W. et al. Arctic freshwater export: status, mechanisms, and prospects. *Glob. Planet. Change* **125**, 13–35 (2015).

Methods

Historical hydrographic data

We have assembled an extensive historical hydrographic dataset that consists of temperature and salinity profiles measured by ships, expendable probes, ice-tethered profilers and gliders, from the following four sources: (a) the World Ocean Database 2018, obtained from the National Centers for Environmental Information, spanning from 1849 to 2020 in the Arctic Ocean; (b) the Unified Database for Arctic and Subarctic Hydrography, which is a composite dataset of salinity and temperature profiles in the domain north of 65° N covering 1980–2015 (ref. 39); (c) a collection of hydrographic data from the Chukchi Sea from various international sources, spanning 1922–2019 (ref. 40); and (d) additional hydrographic profiles in the BG from the Arctic Data Center and the Beaufort Gyre Exploration Project[1]. We removed duplicate profiles. In this study, we focus on the data from 2003 to 2019 (Extended Data Fig. 5).

Although the datasets listed above have been previously scrutinized, further quality control and error checking were applied as described in ref. 17. To construct maps of the variables, we gridded the data using a Laplacian-spline interpolation scheme[41] with a grid spacing of 1° in longitude and 0.25° in latitude. Further gridding was done for salinity bins, spanning the range 28–34 with an interval of 0.2, and trends were computed using this gridded product.

DOT

We employ the monthly altimetry-derived DOT (sea surface height referenced to the geoid) product from 2003 to 2014, with a resolution of 0.75° × 0.25° (ref. 42). Following the previous methodology, we extended the time series using the original processing algorithm for the full CryoSat-2 time series and up to 88° N. The algorithm is described briefly here, with the reader referred to ref. 42 for the full technical description. Satellite open ocean surface elevations were obtained from the low-resolution mode (LRM) and synthetic aperture radar (SAR) ocean modes, and from leads (cracks in the sea ice cover) from SAR ice and SAR interferometric modes (SARIn). The UCL13 mean sea surface product was used to calculate the sea level anomaly (SLA) for all four modes. A monthly mean SLA offset of LRM to SAR ocean, SAR ocean to SAR lead and SAR lead to SARIn lead, from coincident measurements on a 100-km-resolution grid, was calculated to remove mode bias compared with the LRM mode SLA. Following this, the GOCO03s geoid was used to calculate the DOT, removing the bias from the SLA calculation. The individual DOT and SLA measurements were collected onto the 0.75° × 0.25° grid with outliers above and below the 10th percentiles removed. A smoothed DOT using a 100 km Gaussian kernel was created with the gradient taken to give geostrophic surface currents. Following the repeat usage of the algorithm from ref. 42, differences between the original and updated datasets over the period 2011–2014 are less than 1%.

Moorings

Japan Agency for Marine-Earth Science and Technology (JAMSTEC) has maintained three moorings across the mouth of Barrow Canyon (Extended Data Fig. 5) since 2001, except for the four years of June 2004–September 2005, September 2008–August 2010 and October 2013–August 2014 (ref. 15). The central mooring is situated in the centre of Barrow Canyon, and the other two moorings are located on the eastern and western flanks. All three moorings were equipped with MicroCATs for measuring hourly temperature and salinity, and acoustic doppler current profilers (ADCPs) or point current meters for measuring velocities every 0.25–2 hours. The ADCP data have bin sizes between 4 and 8 m in the vertical. The accuracies of the sensors are 0.001 °C for temperature, 0.01 for salinity and 0.01 m s^{-1} for velocity[20]. The temperature, salinity and velocity are gridded along the section across the mouth of Barrow Canyon, with a grid size of 2 km in the horizontal and 2 m in the vertical. Owing to the lack of data in the upper 50 m, the gridded vertical sections only cover the portion of the water column deeper than $S = 31$. The volume of water fluxed across the section in each year is calculated by the mean velocity, cross-sectional area and time. In this study, we use the data from 2003 to 2019, consistent with the DOT data. The climatological mean DOT for this period is shown in Extended Data Fig. 1.

Reanalysis data

We compute wind stress curl using the hourly wind data from the ERA5 reanalysis, provided by the European Centre for Medium-Range Weather Forecasts (ECMWF)[43]. The ERA5 is the fifth generation ECMWF reanalysis product with a grid spacing of 0.25° × 0.25°. It has been widely used in previous high-latitude studies[17].

We make use of the velocity data in the CHL from GLORYS12 (ref. 44), obtained from the Copernicus Marine and Environment Monitoring Service (CMEMS). GLORYS12 is a NEMO (Nucleus for European Modelling of the Ocean)-based reanalysis that assimilates satellite observations and historical hydrographic profiles. It has a horizontal resolution of 1/12° and 50 vertical levels with increased resolution in the upper layer (1–30 m interval in the upper 200 m).

We compared the GLORYS12 velocities with mooring data at various locations in the western Arctic. Extended Data Fig. 3 shows the two examples of the comparison: in the vicinity of the Bering Strait[45] ($r = 0.76$, $P < 0.01$; and at shelfbreak in the western Beaufort Sea[16] ($r = 0.54$, $P < 0.01$). The good agreements motivated us to use the reanalysis velocity field to carry out the Lagrangian particle experiments in the study.

GRACE

We use the monthly equivalent water thickness from the Gravity Recovery and Climate Experiment (GRACE) and the follow on (GRACE-FO) Mascon solutions (release-06, version 2) from the Center for Space Research[46] in combination with the DOT data to estimate the FWC (see below). There are 31 months of gaps in the two-decade record due to the satellite's regular battery management. To fill each of the gaps, we apply a five-month weighting window centred at the month in question[42]. This technique was not applicable for 2017–2018, when there were successive gap months. In this case, we filled each gap with the mean of the same month from the year before and after. The GRACE data have a spatial resolution of 0.25°, and were interpolated onto the same grid as the DOT data.

Vertical structure of the water column

The different vertical layers considered in the study are depicted in Extended Data Fig. 6 using mean hydrographic profiles from the BG. The base of surface layer is defined as the depth at which the potential density difference exceeds 0.125 kg m^{-3} from the mean density in the upper 10 m (ref. 47). Below that, the halocline in the Canada Basin consists of the warm halocline layer and the CHL (ref. 18). The warm halocline layer is between the base of surface layer and the first minimum in buoyancy frequency below the maximum value. Below this is the cold halocline, the base of which is determined using the ratio $R = \alpha\Delta T/\beta\Delta S$, where T is the temperature, S is the salinity, α is the thermal expansion coefficient and β is the haline contraction coefficient[48]. In particular, the depth where $R = 0.05$, at which point the vertical density gradient is mainly due to the salinity gradient, is taken to be the base of cold halocline. The Atlantic water layer resides below this.

FWC

The FWC is calculated as $\mathrm{FWC}_1 = \int_h^0 \frac{(S_r - S(z))}{S_r} \mathrm{d}z$, applied using the historical hydrographic data over the BG region[2]. The reference salinity S_r is 34.8 at the corresponding depth h, and $S(z)$ is the depth-dependent salinity. For each year, we interpolated the FWC_1 within the BG region using the Laplacian-spline interpolation[41], with a resolution of 1° in the longitude and 0.25° in the latitude, and then computed the mean value.

We also use the DOT and GRACE data to estimate the annual FWC following the methodology used in previous studies[5,7,42], $\mathrm{FWC}_2 = \frac{S_r - S_1}{S_r}\Delta h$,

where S_1 is the salinity in the upper layer. In particular, as a simplification, the water column in the BG can be considered as two homogeneous layers: a lighter layer with density $\rho_1 = 1{,}022\ \mathrm{kg\ m^{-3}}$ atop a denser layer with density $\rho_2 = 1{,}028\ \mathrm{kg\ m^{-3}}$. Variations in the FWC alter the thickness of the upper layer $\Delta h = \eta\left(1 + \frac{\rho_1}{\rho_2 - \rho_1}\right) - \frac{\Delta m}{\rho_2 - \rho_1}$, which is reflected by the DOT (η) and ocean mass (Δm). The Δm is estimated using the GRACE equivalent water thickness multiplied by the water density. The mean freshwater volume over the BG region is computed as the spatial mean FWC (FWC_1 or FWC_2) multiplied by the area of the BG region.

Lagrangian particle experiments

The two Lagrangian particle experiments carried out in the study make use of the GLORYS12 reanalysis velocity data. We first computed the annual mean velocity in the CHL for the two extreme years of 2011 and 2019. For each experiment, we then released 150 particles along the 100 m isobath within the CHL in the CS/WBS and EBS, and computed the trajectories given the annual mean velocity field. At each time step, the velocity at the nearest grid point to where the particle is located is used to compute the distance travelled over one day. This procedure is iterated for a year.

Data availability

The historical hydrographic data are obtained from the following sources: (1) Unified Database for Arctic and Subarctic Hydrography (https://doi.pangaea.de/10.1594/PANGAEA.872931); (2) World Ocean Database 2018 (https://www.ncei.noaa.gov/products/world-ocean-database); (3) Arctic Data Center (https://arcticdata.io/catalog/data); (4) Beaufort Gyre Exploration Project (https://www2.whoi.edu/site/beaufortgyre/data/data-overview/); (5) Pacific Marine Environmental Laboratory (https://www.pmel.noaa.gov/data-links); (6) NOAA Alaska Fisheries Science Center (https://data.eol.ucar.edu/dataset/); (7) University of Alaska Fairbanks Institute of Marine Science (available at the Arctic Ocean Observing System, http://www.aoos.org); (8) Fisheries and Oceans Canada's Institute of Ocean Sciences (https://www.dfo-mpo.gc.ca/science/publications/index-eng.htm); (9) JAMSTEC (http://www.godac.jamstec.go.jp/darwin/e/); and (10) Korea Polar Data Center (https://kpdcopen.kopri.re.kr). The dynamic ocean topography data produced by ref. 42 and the updated dynamic ocean topography data from 2011 to 2019 are available at http://www.cpom.ucl.ac.uk/dynamic_topography/. The GRACE data can be accessed via https://sealevel.nasa.gov/data/dataset/?identifier=SLCP_CSR-RL06-Mascons-v02_RL06_v02. The ERA5 reanalysis data can be obtained from the ECMWF (https://rmets.onlinelibrary.wiley.com/doi/10.1002/qj.3803). The GLORYS12 reanalysis is available at the Copernicus Marine and Environment Monitoring Service (https://data.marine.copernicus.eu/product/GLOBAL_MULTIYEAR_PHY_001_030/description). The JAMSTEC mooring data at the mouth of the Barrow Canyon from 2003 to 2019 are available at https://www.jamstec.go.jp/iace/e/report/. The monthly time series of the Arctic Oscillation index is obtained from NOAA's Climate Prediction Center (https://www.cpc.ncep.noaa.gov/products/precip/CWlink/daily_ao_index/ao.shtml). The bathymetry data used in the study are from the International Bathymetric Chart of the Arctic Ocean version 3 (ref. 49) (https://www.gebco.net/about_us/committees_and_groups/scrum/ibcao/ibcao_v3.html).

Code availability

The MATLAB scripts used to compute the freshwater content and to calculate the Lagrangian particle trajectories can be accessed upon request to the corresponding author.

References

39. Behrendt, A., Sumata, H., Rabe, B. & Schauer, U. UDASH–Unified Database for Arctic and Subarctic Hydrography. *Earth Syst. Sci. Data* **10**, 1119–1138 (2018).
40. Danielson, S. et al. Manifestation and consequences of warming and altered heat fluxes over the Bering and Chukchi sea continental shelves. *Deep Sea Res. II* **177**, 104781 (2020).
41. Smith, W. & Wessel, P. Gridding with continuous curvature splines in tension. *Geophysics* **55**, 293–305 (1990).
42. Armitage, T. W. et al. Arctic sea surface height variability and change from satellite radar altimetry and GRACE, 2003–2014. *J. Geophys. Res. Oceans* **121**, 4303–4322 (2016).
43. Hersbach, H. *Operational Global Reanalysis: Progress, Future Directions and Synergies with NWP* (ECMWF, 2018).
44. Lellouche, J.-M. et al. The Copernicus global 1/12° oceanic and sea ice GLORYS12 reanalysis. *Front. Earth Sci.* **9**, 585 (2021).
45. Woodgate, R. A. Increases in the Pacific inflow to the Arctic from 1990 to 2015, and insights into seasonal trends and driving mechanisms from year-round Bering Strait mooring data. *Prog. Oceanogr.* **160**, 124–154 (2018).
46. Save, H. et al. High resolution CSR GRACE RL05 mascons. *J. Geophys. Res. Solid Earth* **121**, 7547–7569 (2016).
47. Marshall, J. & Radko, T. Residual-mean solutions for the Antarctic Circumpolar Current and its associated overturning circulation. *J. Phys. Oceanogr.* **33**, 2341–2354 (2003).
48. Bourgain, P. & Gascard, J.-C. The Arctic Ocean halocline and its interannual variability from 1997 to 2008. *Deep Sea Res. I* **58**, 745–756 (2011).
49. Jakobsson, M. et al. The International Bathymetric Chart of the Arctic Ocean (IBCAO) version 3.0. *Geophys. Res. Lett.* **39**, L12609 (2012).

Acknowledgements

Funding for the study was provided by National Science Foundation grant OPP-1733564 and National Oceanic and Atmospheric Administration grant NA19OAR4320074 (P.L., R.S.P.); Shanghai Pujiang Program 22PJ1406400 and Shanghai Frontiers Science Center of Polar Science (P.L.); European Space Agency Project ESA/AO/1-9132/17/NL/MP and ESA/AO/1-10061/19/I-EF and Natural Environment Research Council NE/T000546/1 and NE/X004643/1 (M.T.); and Arctic Challenge for Sustainability projects ArCS and ArCSII of the Ministry of Education, Culture, Sports, Science and Technology (M.I., T.K.).

Author contributions

P.L. led the data analysis and resulting interpretation, with assistance from all co-authors. P.L. and R.S.P. wrote the manuscript with input from all co-authors. H.H. and M.T. produced the updated dynamic ocean topography data from 2011 to 2019. M.I. and T.K. provided the long-term data from the mooring array at the mouth of Barrow Canyon.

Competing interests

The authors declare no competing interests.

Additional information

Extended data is available for this paper at https://doi.org/10.1038/s41561-023-01184-5.

Correspondence and requests for materials should be addressed to Peigen Lin.

Peer review information *Nature Geoscience* thanks the anonymous reviewers for their contribution to the peer review of this work. Primary Handling Editors: Rebecca Neely and Tom Richardson, in collaboration with the *Nature Geoscience* team.

https://doi.org/10.1038/s41561-023-01184-5

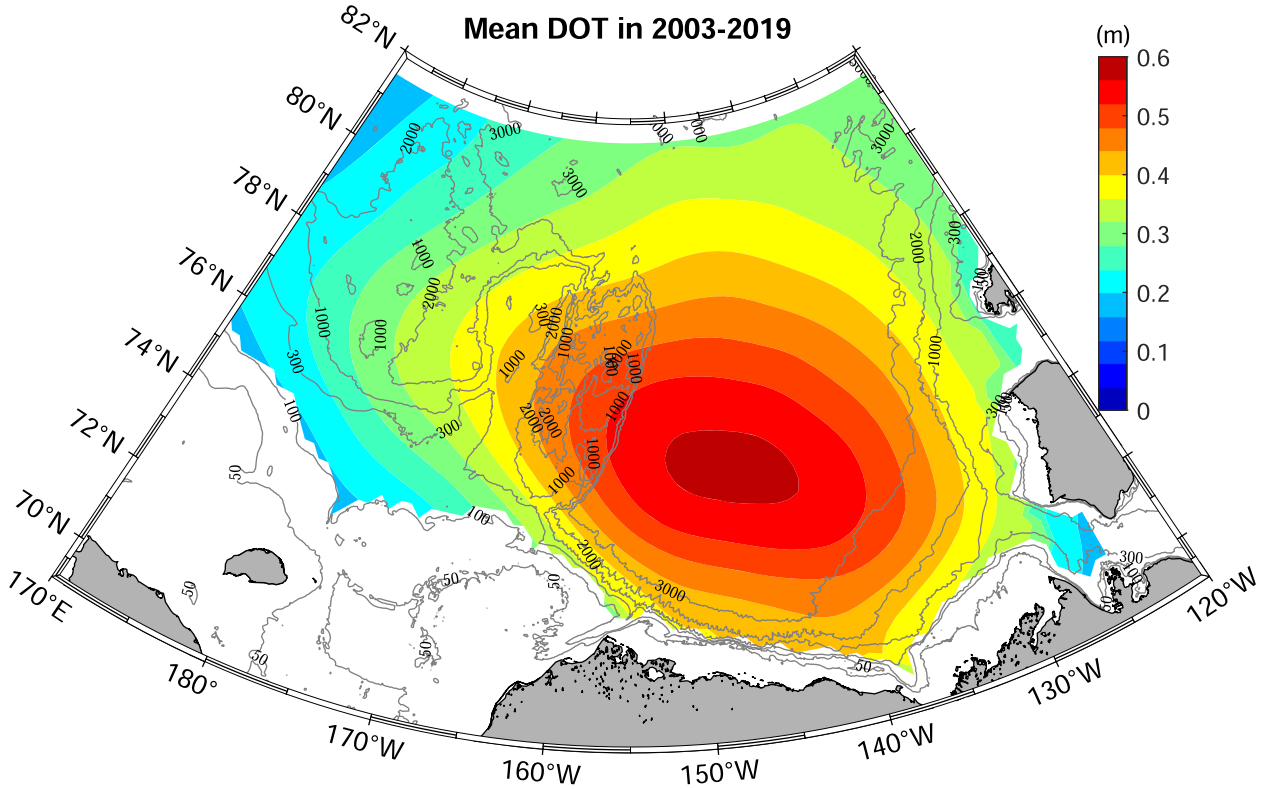

Extended Data Fig. 1 | Climatological mean dynamic ocean topography (DOT) from 2003-2019. The data for water depths shallower than 100 m are not shown.

https://doi.org/10.1038/s41561-023-01184-5

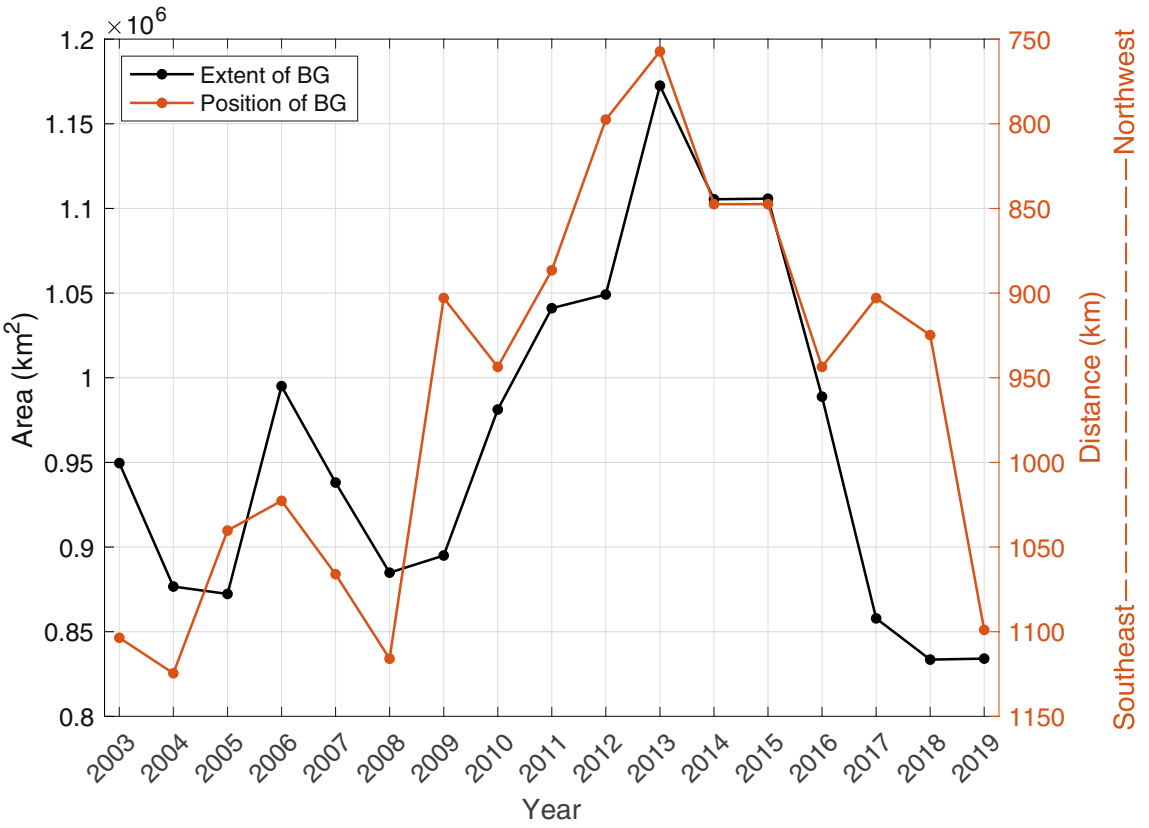

Extended Data Fig. 2 | Variations of extent versus position of the Beaufort Gyre. The extent of Beaufort Gyre (BG) is estimated as the area within the isoline of 0.6 × maximum DOT for each year (the result is not sensitive to the fraction used) (black curve). As in Fig. 4a, the position of Beaufort Gyre is represented by the distance of the projected core along the line in Fig. 2c (red curve).

https://doi.org/10.1038/s41561-023-01184-5

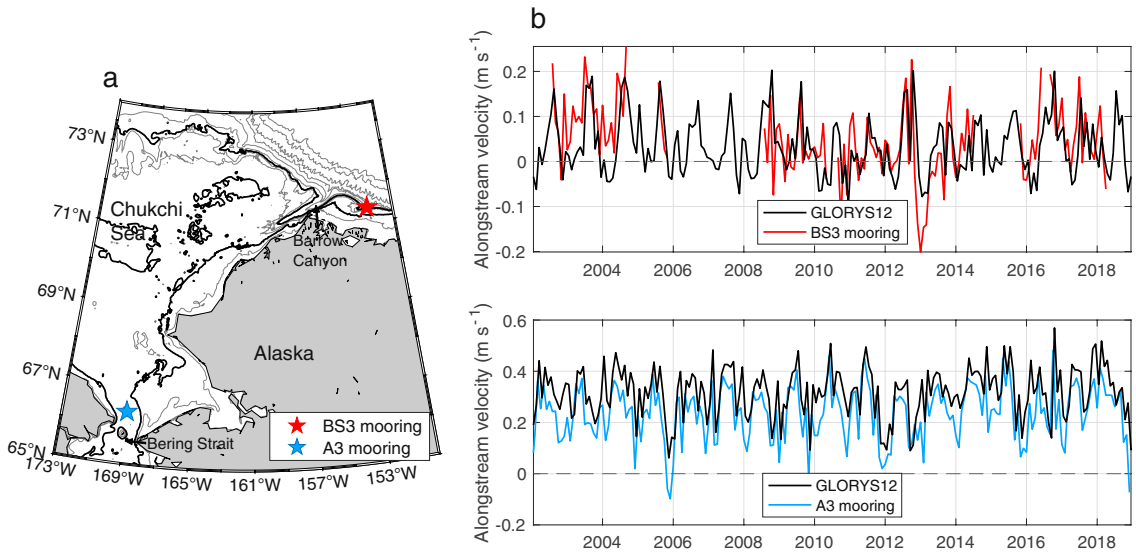

Extended Data Fig. 3 | Comparison of GLORYS12 reanalysis velocities versus mooring data. a, The location of the moorings at the shelfbreak of western Beaufort Sea (BS3, red star) and in the vicinity of Bering Strait (A3, blue star). **b**, Timeseries of alongstream velocity of GLORYS12 (black curve) versus BS3 mooring (red curve), and GLORYS12 versus A3 mooring (blue curve).

https://doi.org/10.1038/s41561-023-01184-5

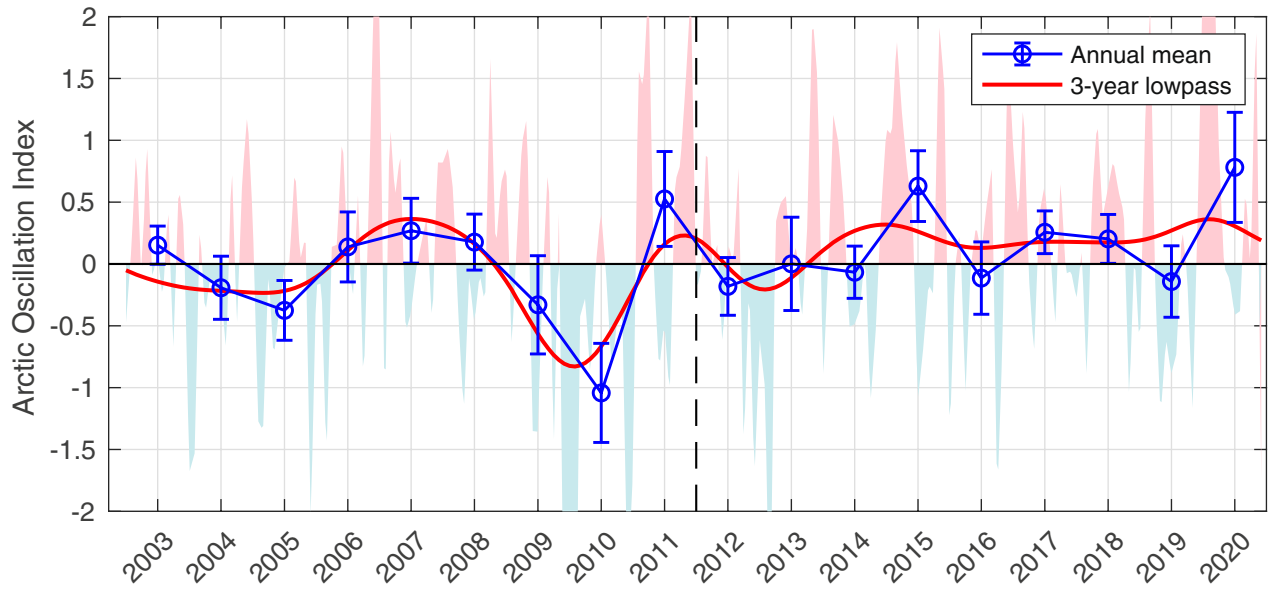

Extended Data Fig. 4 | Timeseries of the Arctic Oscillation Index. The shading denotes the monthly values; the annual averages are the blue symbols/curve, including the standard errors; the 3-year lowpassed timeseries is the red curve. The monthly timeseries is obtained from NOAA's Climate Prediction Center. The standard error is the standard deviation divided by square root of the degrees of freedom (=12) for each year.

https://doi.org/10.1038/s41561-023-01184-5

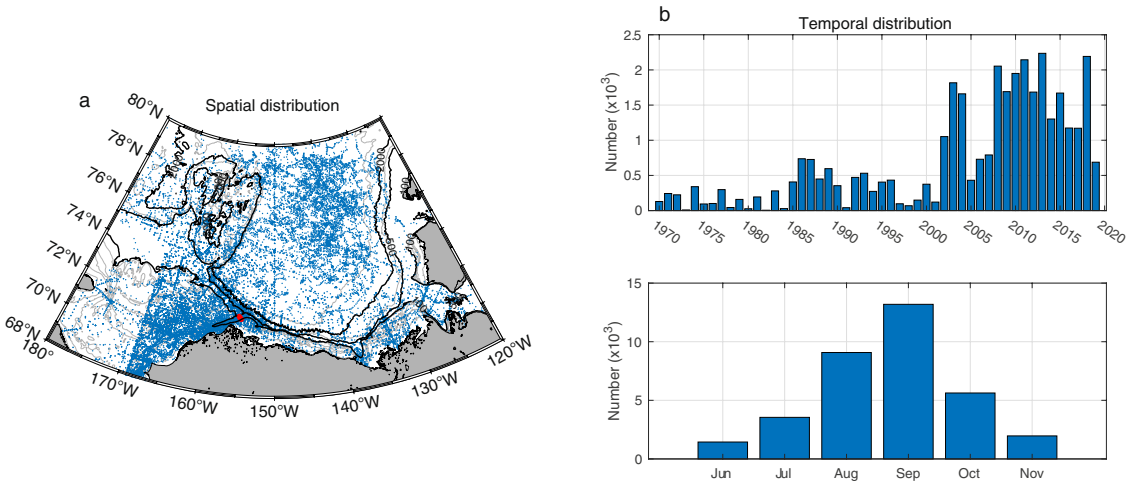

Extended Data Fig. 5 | Data coverage of the composite historical hydrographic dataset. a, Geographical map of the data distribution, including the location of the Barrow Canyon mooring array (red stars). **b**, The number of profiles in each year corresponding to the warm months and the monthly distribution.

https://doi.org/10.1038/s41561-023-01184-5

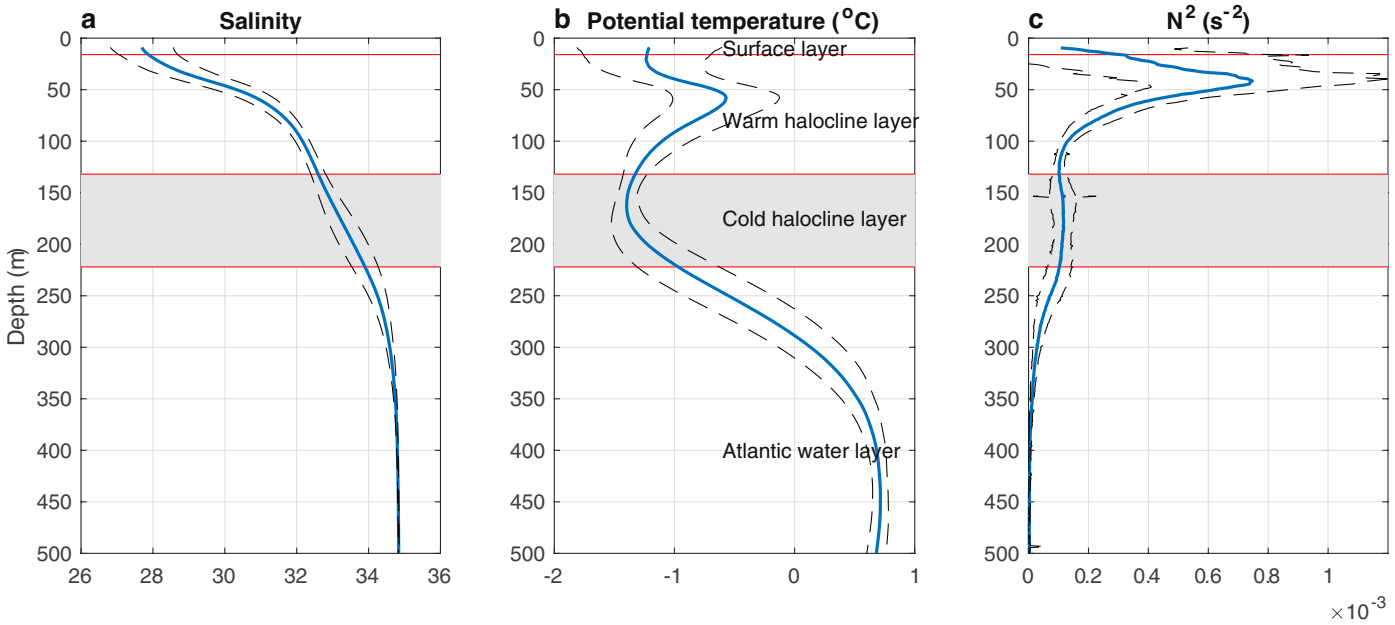

Extended Data Fig. 6 | Vertical structure of water column in the Beaufort Gyre region. Mean profiles of **a**, salinity, **b**, potential temperature (°C), and **c**, buoyancy frequency (N^2, s^{-2}) in the upper 500 m for the time period 2003-2019. The dashed curves denote the standard deviation. The four layers delimited by the red solid lines are (from the surface downward): the surface layer, the warm halocline layer, the cold halocline layer (shaded), and the Atlantic water layer (see Methods for the definitions).